Application of the Space-Time Conservation Element and Solution Element Method to Shock-Tube Problem

Xiao-Yen Wang, Chuen-Yen Chow
Department of Aerospace Engineering Sciences
University of Colorado at Boulder
Boulder, Colorado 80309-0429
and
Sin-Chung Chang
National Aeronautics and Space Adminitration
Lewis Research Center
Cleveland, Ohio 44135

Abstract

An Euler solver based on the method of space-time conservation element and solution element is used in this paper to simulate shock-tube flows involving shock waves, contact discontinuities, expansion waves and their intersections. Seven test problems are considered to examine the capability of this method. The numerical results, when compared with exact solutions and/or numerical solutions by other methods, indicate that the present method can accurately resolve strong shock and contact discontinuities without using any ad hoc techniques which are used only at the neighborhood of a discontinuity.

Introduction

The method of space-time conservation element and solution element (to be abbreviated later as the CE/SE method) is a numerical method developed recently by Chang[1] for solving conservation laws governing the motion of fluids. This new method differs substantially in both concept and methodology from the well-established traditional methods such as the finite difference, finite volume, finite element and spectral methods. It is conceived and designed to overcome some of the major shortcomings of the traditional methods.

The development of this new method is guided by several basic requirements. They are: (i) to enforce both local and global flux conservation in space and time with flux evaluation at an interface of two conservation elements being an integral part of the solution procedure and requiring no interpolation or extrapolation; (ii) to use local discrete variables such that the set of variables in any one of the numerical equations to be solved is associated with a set of immediately neighboring solution elements; (iii) space and time are unified and treated on the same footing; (iv) mesh values of dependent variables and their derivatives are considered as independent variables to be solved simultaneously; (v) to minimize numerical diffusion, a numerical analogue should be constructed, as much as possible, to be compatible with the space-time invariant properties of the corresponding physical equations; and (vi) to exclude the use of the characteristics-based techniques, and to avoid the use of ad hoc techniques as much as possible. It was shown in [1] that the above requirments can be met with a simple unified numerical framework.

One of the numerical schemes developed in [1] is an Euler solver for solving the one-dimensional unsteady Euler equations. It was used to obtain accurate flow solutions involving an infinitely long shock tube.

In this work, the above Euler solver is extended and applied to more complex flow problems involving shock tubes of finite or infinite length. Shock-tube flows represent a class of particularly interesting test cases that have exact solutions in the presence of shock waves, contact discontinuities, expansion fans and even their reflection and intersection when the tube length is finite. The ability to generate

numerical algorithms which allow a high resolution of discontinuities, such as shock waves and contact discontinuities, without numerical oscillations is an important requirement of a method since the appearance of such discontinuities is a frequent and essential phenomenon of high-speed inviscid flows.

In the following sections, the governing equations and numerical scheme are first summarized from [1], which is then followed by a detailed description of each of the test cases.

2. Governing Equations

The one-dimensional unsteady Euler equations of a perfect gas can be expressed as

$$\frac{\partial u_m}{\partial t} + \frac{\partial f_m}{\partial x} = 0, \quad m = 1, 2, 3 \tag{2.1}$$

where

$$u_1 = \rho, \quad u_2 = \rho v, \quad u_3 = \frac{p}{\gamma - 1} + \frac{1}{2}\rho v^2 \tag{2.2}$$

$$f_1 = u_2 \tag{2.3}$$

$$f_2 = (\gamma - 1)u_3 + \frac{1}{2}(3 - \gamma)\frac{(u_2)^2}{u_1} \tag{2.4}$$

$$f_3 = \gamma\frac{u_2 u_3}{u_1} - \frac{1}{2}(\gamma - 1)\frac{(u_2)^3}{(u_1)^2} \tag{2.5}$$

with ρ, v, p and γ being the density, velocity, static pressure and constant specfic heat ratio, respectively.

Let $x_1 = x$, and $x_2 = t$ be considered as the coordinates of a two-dimensional Euclidean space E_2. By using Gauss' divergence theorem in the space-time E_2, it can be shown that Eq. (2.1) is the differential form of the integral conservation law

$$\oint_{S(V)} \vec{h}_m \cdot d\vec{s} = 0, \quad m = 1, 2, 3. \tag{2.6}$$

here (i) $S(V)$ is the boundary of an arbitrary space-time region V in E_2, (ii) $d\vec{s} = d\sigma\,\vec{n}$ with $d\sigma$ and $\vec{n}$, respectively, being the area and the outward unit normal of a surface element on $S(V)$, and (iii) $\vec{h}_m = (f_m, u_m)$, $m = 1, 2, 3$, are the space-time mass,

momentum, and energy current density vectors, respectively. Note that (i) $\vec{h}_m \cdot d\vec{s}$ is the space-time flux of $\vec{h}_m$ leaving the region V through the surface element $d\vec{s}$, and (ii) all mathematical operations can be carried out as though E_2 were an ordinary two-dimensional Euclidean space.

3. Euler Solver

3(a). Marching Schemes for Interior Mesh Points

Let Ω denote the set of mesh points (j,n) in E_2 (dots in Fig. 1(a)) where $n = 0, \pm 1/2, \pm 1, \pm 3/2, \pm 2, \pm 5/2, \cdots$, and, for each n, $j = n \pm 1/2, n \pm 3/2, n \pm 5/2, \cdots$. There is a solution element (SE) associated with each $(j,n) \in \Omega$. Let the solution element SE(j,n) be the interior of the space-time region bounded by a dashed curve depicted in Fig. 1(b). It includes a horizontal line segment, a vertical line segment, and their immediate neighborhood. For the following discussions, the exact size of the neighborhood does not matter.

For any $(x,t) \in$ SE(j,n), $u_m(x,t), f_m(x,t)$, and $\vec{h}_m(x,t)$ are approximated by $u_m^*(x,t;j,n)$, $f_m^*(x,t;j,n)$, and $\vec{h}_m^*(x,t;j,n)$, respectively. They will be defined shortly. Let

$$u_m^*(x,t;j,n) = (u_m)_j^n + (u_{mx})_j^n(x - x_j) + (u_{mt})_j^n(t - t^n) \tag{3.1}$$

where $(u_m)_j^n, (u_{mx})_j^n$ and $(u_{mt})_j^n$ are constants in SE(j,n). They can be considered as the numerical analogues of the values of $u_m, \dfrac{\partial u_m}{\partial x}$ and $\dfrac{\partial u_m}{\partial t}$ at (x_j, t^n), respectively. Let

$$f_{m,k} = \frac{\partial f_m}{\partial u_k}, \quad m,k = 1,2,3 \tag{3.2}$$

Let $(f_m)_j^n$ and $(f_{m,k})_j^n$ denote the values of f_m and $f_{m,k}$, respectively, when u_m, $m = 1,2,3$, respectively, assume the values of $(u_m)_j^n$, $m = 1,2,3$. Let

$$(f_{mx})_j^n = \sum_{k=1}^{3} (f_{m,k})_j^n (u_{kx})_j^n \tag{3.3}$$

and

$$(f_{mt})_j^n = \sum_{k=1}^{3} (f_{m,k})_j^n (u_{kt})_j^n \tag{3.4}$$

It is explained in [1] that $(f_{mx})_j^n$ and $(f_{mt})_j^n$ can be considered as the numerical analogues of the values of $\frac{\partial f_m}{\partial x}$ and $\frac{\partial f_m}{\partial t}$ at (x_j, t^n), respectively. As a result, it is assumed that

$$f_m^*(x,t;j,n) = (f_m)_j^n + (f_{mx})_j^n(x - x_j) + (f_{mt})_j^n(t - t^n) \tag{3.5}$$

Because $\vec{h}_m = (f_m, u_m)$, it is also assumed that

$$\vec{h}_m^*(x,t;j,n) = (f_m^*(x,t;j,n), u_m^*(x,t;j,n)) \tag{3.6}$$

Note that, by their definitions, (i) $(f_m)_j^n$ and $(f_{m,k})_j^n$, $m = 1,2,3$, are functions of $(u_m)_j^n$, $m = 1,2,3$, (ii) $(f_{mx})_j^n$, $m = 1,2,3$, are functions of $(u_m)_j^n$ and $(u_{mx})_j^n$, $m = 1,2,3$, and (iii) $(f_{mt})_j^n$ are functions of $(u_m)_j^n$ and $(u_{mt})_j^n$, $m = 1,2,3$.

Moreover, it is assumed that, for any $(x,t) \in \mathrm{SE}(j,n)$, $u_m = u_m^*(x,t;j,n)$ and $f_m = f_m^*(x,t;j,n)$ satisfy (2.1), i.e.,

$$\frac{\partial u_m^*(x,t;j,n)}{\partial t} + \frac{\partial f_m^*(x,t;j,n)}{\partial x} = 0 \tag{3.7}$$

According to (3.1) and (3.5), Eq. (3.7) is equivalent to

$$(u_{mt})_j^n = -(f_{mx})_j^n \tag{3.8}$$

Because $(f_{mx})_j^n$ are functions of $(u_m)_j^n$ and $(u_{mx})_j^n$, Eq. (3.8) implies that $(u_{mt})_j^n$ are also functions of $(u_m)_j^n$ and $(u_{mx})_j^n$. From this result and the facts stated following Eq. (3.6), one concludes that $(u_{mt})_j^n, (f_m)_j^n, (f_{mx})_j^n$ and $(f_{mt})_j^n$ are functions of $(u_m)_j^n$ and $(u_{mx})_j^n$. As a result, $(u_m)_j^n$ and $(u_{mx})_j^n$, $m = 1,2,3$, are the only independent discrete variables needed to be solved in the current marching scheme.

The main marching scheme developed in [1] is defined by

$$(u_m)_j^n = \frac{1}{2}\left[(u_m)_{j-1/2}^{n-1/2} + (u_m)_{j+1/2}^{n-1/2} + (s_m)_{j-1/2}^{n-1/2} - (s_m)_{j+1/2}^{n-1/2}\right] \tag{3.9}$$

and

$$(u_{mx})_j^n = (u_{mx}^c)_j^n + (2\epsilon - 1)(du_{mx})_j^n \tag{3.10}$$

where ϵ is a parameter that controls numerical diffusion. Also, for all $(j,n) \in \Omega$:

$$(s_m)_j^n = \frac{\Delta x}{4}(u_{mx})_j^n + \frac{\Delta t}{\Delta x}(f_m)_j^n + \frac{(\Delta t)^2}{4\Delta x}(f_{mt})_j^n \tag{3.11}$$

$$(du_{mx})_j^n = \frac{1}{2}\left[(u_{mx})_{j+1/2}^{n-1/2} + (u_{mx})_{j-1/2}^{n-1/2}\right] - \frac{(u_m)_{j+1/2}^{n-1/2} - (u_m)_{j-1/2}^{n-1/2}}{\Delta x} \tag{3.12}$$

$$(u_{mx}^c)_j^n = \frac{(u_m')_{j+1/2}^n - (u_m')_{j-1/2}^n}{\Delta x} \tag{3.13}$$

with

$$(u_m')_{j\pm1/2}^n = (u_m)_{j\pm1/2}^{n-1/2} + \frac{\Delta t}{2}(u_{mt})_{j\pm1/2}^{n-1/2} \tag{3.14}$$

Let (i)

$$(u_{mx_\pm})_j^n = \pm\frac{(u_m')_{j\pm1/2}^n - (u_m)_j^n}{\Delta x/2} \tag{3.15}$$

(ii) $\alpha \geq 0$ be an adjustable parameter, and (iii) the function W_0 be defined by

$$W_0(0,0;\alpha) = 0 \tag{3.16}$$

and

$$W_0(x_-,x_+;\alpha) = \frac{|x_+|^\alpha x_- + |x_-|^\alpha x_+}{|x_+|^\alpha + |x_-|^\alpha} \quad (|x_+|^\alpha + |x_-|^\alpha > 0) \tag{3.17}$$

Then the main scheme can be modified by replacing $(u_{mx}^c)_j^n$ with

$$(u_{mx}^{w_0})_j^n = W_0\left[(u_{mx_-})_j^n, (u_{mx_+})_j^n; \alpha\right] \tag{3.18}$$

This modification is introduced such that numerical oscillations near a discontinuity can be suppressed without smearing the discontinuity. It also has the advantage that the modification has no discernable effect on the smooth part of the solution [1].

3(b). Marching Scheme for Boundary Mesh Points

The marching schemes defined in Sec. 3(a) are applicable only for interior points $(j,n) \in \Omega$. The boundary mesh points enter into the picture when shock-tube problems with closed ends are considered later in the current paper. As a preliminary for deriving the marching scheme for boundary mesh points, we shall review the concept of conservation element introduced in [1].

Let space-time E_2 be divided into nonoverlapping rectangular regions referred to as conservation elements (CEs). As depicted in Figs. 1(c)–(e), conservation elements of three different types enter the current discussion. Conservation element $CE_-(j,n)$ is associated with a right-boundary mesh point $(j,n) \in \Omega$. Conservation element $CE_+(j,n)$ is associated with a left-boundary mesh point $(j,n) \in \Omega$. Finally, conservation element $CE(j,n)$ is associated with an interior mesh point. Note that (i) the CEs associated with all $(j,n) \in \Omega$ fill the entire computation domain, (ii) The boundary of $CE_-(j,n)$ ($CE_+(j,n)$) is formed by the subsets of $SE(j,n)$ and $SE(j-1/2,n-1/2)$ ($SE(j+1/2,n-1/2)$), and (iii) the boundary of $CE(j,n)$ is formed by the subsets of $SE(j,n)$, $SE(j-1/2,n-1/2)$ and $SE(j+1/2,n-1/2)$.

We assumed that (i)

$$\oint_{S(CE(j,n))} \vec{h}_m^* \cdot d\vec{s} = 0 \tag{3.19}$$

for any interior mesh point $(j,n) \in \Omega$, (ii)

$$\oint_{S(CE_-(j,n))} \vec{h}_m^* \cdot d\vec{s} = 0 \tag{3.20}$$

for any right-boundary mesh point $(j,n) \in \Omega$, and (iii)

$$\oint_{S(CE_+(j,n))} \vec{h}_m^* \cdot d\vec{s} = 0 \tag{3.21}$$

for any left-boundary mesh point $(j,n) \in \Omega$. Equations. (3.19)–(3.21) imply that, for $m = 1,2,3$, the total flux leaving the boundary of any conservation element is zero. Moreover, because the flux at any interface separating two neighboring CEs is calculated using the information from a single SE, the local conservation conditions Eqs. (3.19)–(3.21) will lead to a global conservation relation, i.e., the total flux leaving the boundary of any space-time region that is the union of any combination of CEs will also vanish.

With the aid of Eqs. (4.24) and (4.25) in [1], Eqs. (3.19)–(3.21) imply, respectively, (i) Eq. (3.9), which is valid for an interior mesh point $(j,n) \in \Omega$, (ii)

$$-\frac{\Delta x}{4}(u_{mx})_j^n + \frac{\Delta t}{\Delta x}(f_m)_j^n - \frac{(\Delta t)^2}{4\Delta x}(f_{mt})_j^n + (u_m)_j^n = (u_m)_{j-1/2}^{n-1/2} + (s_m)_{j-1/2}^{n-1/2} \tag{3.22}$$

where (j,n) is a right-boundary mesh point $\in \Omega$, and (iii)

$$\frac{\Delta x}{4}(u_{mx})_j^n - \frac{\Delta t}{\Delta x}(f_m)_j^n + \frac{(\Delta t)^2}{4\Delta x}(f_{mt})_j^n + (u_m)_j^n = (u_m)_{j+1/2}^{n-1/2} - (s_m)_{j+1/2}^{n-1/2} \tag{3.23}$$

where (j,n) is a left-boundary mesh point $\in \Omega$. Equation (3.9) is a part of the marching schemes defined in Sec. 3(a). Note that derivation of Eq. (3.10) or its modified version involves considerations other than flux conservation. The marching schemes for boundary mesh points will be derived using Eqs. (3.22) and (3.23), and the appropriate boundary conditions to be imposed.

It is assumed that, for all $t > 0$,

$$v = 0, \quad \frac{\partial \rho}{\partial x} = 0, \quad \frac{\partial p}{\partial x} = 0 \tag{3.24}$$

at a closed end. Using Eqs. (2.1)–(2.5) and (3.24), one has

$$u_2 = 0, \quad f_1 = f_3 = 0, \quad f_2 = (\gamma - 1)u_3 \tag{3.25}$$

$$\frac{\partial f_1}{\partial t} = \frac{\partial f_3}{\partial t} = 0, \quad \frac{\partial f_2}{\partial t} = -\gamma(\gamma - 1)\frac{u_3}{u_1}\frac{\partial u_2}{\partial x} \tag{3.26}$$

and

$$\frac{\partial u_1}{\partial x} = \frac{\partial u_3}{\partial x} = 0 \tag{3.27}$$

at a closed end. It is assumed that the numerical analogues of Eqs. (3.25)–(3.27) are also valid, i.e.,

$$(u_2)_j^n = 0, \quad (f_1)_j^n = (f_3)_j^n = 0, \quad (f_2)_j^n = (\gamma - 1)(u_3)_j^n \tag{3.28}$$

$$(f_{1t})_j^n = (f_{3t})_j^n = 0, \quad (f_{2t})_j^n = -\gamma(\gamma - 1)(u_3/u_1)_j^n (u_{2x})_j^n \tag{3.29}$$

and

$$(u_{1x})_j^n = (u_{3x})_j^n = 0 \tag{3.30}$$

for any boundary mesh point (j,n). Here $(u_3/u_1)_j^n = (u_3)_j^n/(u_1)_j^n$. Combining Eqs. (3.22), (3.23) and (3.28)–(3.30), one obtains the marching scheme for boundary mesh points, i.e., (i)

$$(u_m)_j^n = \begin{cases} (u_m)_{j-1/2}^{n-1/2} + (s_m)_{j-1/2}^{n-1/2} & \text{for } m = 1,3 \\ 0 & \text{for } m = 2 \end{cases} \tag{3.31}$$

and

$$(u_{mx})_j^n = \begin{cases} \dfrac{(u_m)_{j-1/2}^{n-1/2} + (s_m)_{j-1/2}^{n-1/2} - \dfrac{\Delta t}{\Delta x}(\gamma-1)(u_3)_j^n}{\dfrac{(\Delta t)^2}{4\Delta x}\gamma(\gamma-1)(u_3/u_1)_j^n - \dfrac{\Delta x}{4}} & \text{for } m=2 \\ 0 & \text{for } m=1,3 \end{cases} \tag{3.32}$$

where (j,n) is a right-boundary mesh point, and (ii)

$$(u_m)_j^n = \begin{cases} (u_m)_{j+1/2}^{n-1/2} - (s_m)_{j+1/2}^{n-1/2} & \text{for m=1,3} \\ 0 & \text{for } m=2 \end{cases} \tag{3.33}$$

and

$$(u_{mx})_j^n = \begin{cases} \dfrac{(u_m)_{j+1/2}^{n-1/2} - (s_m)_{j+1/2}^{n-1/2} + \dfrac{\Delta t}{\Delta x}(\gamma-1)(u_3)_j^n}{-\dfrac{(\Delta t)^2}{4\Delta x}\gamma(\gamma-1)(u_3/u_1)_j^n + \dfrac{\Delta x}{4}} & \text{for } m=2 \\ 0 & \text{for } m=1,3 \end{cases} \tag{3.34}$$

where (j,n) is a left-boundary mesh point.

4. Test Problems and discussions

To evaluate the accuracy of the numerical schemes described in the previous sections, the numerical results of seven shock-tube problems are compared with their exact solutions and/or numerical solutions obtained using upwind methods. The shock tubes considered in these experiments are either extended to infinity or having one or two closed ends, $\gamma = 1.4$, and a constant value of $\epsilon = 0.5$ is used for all computations.

Infinitely Long Shock Tubes

Some of the shock-tube problems presented in [3] are solved again here using the present CE/SE Euler solver. In these problems, the shock tube is assumed to be long enough to avoid the reflection of discontinuities. The numerical results are compared to both the exact solutions, plotted using solid lines, and numerical solutions presented in [3].

In the following four problems,the space region [-1,1], unless specified otherwise, is always subdivided into 100 intervals with $\Delta x = 0.02$, while the size of Δt varies depending on the CFL number chosen for each problem. The CFL number is defined as $\frac{\Delta t}{\Delta x}(|v| + c)_{max}$ where $c = \sqrt{\gamma p/\rho}$ is the speed of sound. It is evaluated using the known exact solution. Generally the stability condition is CFL$<$ 1 [1].

A. Strong Shock Waves Propagating in Opposite Directions

The initial conditions at t=0 are:

$$(\rho, p, M) = \begin{cases} (0.1,\ 0.1,\ 15) & \text{for } x < 0 \\ (0.1,\ 0.1,\ -15) & \text{for } x > 0 \end{cases} \tag{4.1}$$

where $M = v/c$.

Two CE/SE solutions at $t = 100\Delta t$ are presented in Figs. 2 and 3. Note that, except in the neighborhood of $x = 0$, these solutions agree almost perfectly with the exact solutions, indicating that the oscillations can be suppressed by increasing the value of α.

In [3], numerical solutions to the above test problem were generated using four upwind schemes. The first is the AUSM (Advection Upstream Splitting Method) scheme. The second is the AUSMV scheme, a flux-Vector-splitting-biased modification of the AUSM scheme. The third is the AUSMD scheme, a flux-Difference-splitting-biased modification of the AUSM scheme. The last is the AUSMDV scheme which is a mixture of the AUSMV and AUSMD schemes. The values of T(temperature), p and ρ generated using the above four methods ($t = 100\Delta t, \Delta x =$ 0.02 and CFL= 1.0), respectively, are plotted against x in Figs. 2(a)-(d) of [3]. Note that T, p and ρ are related by the perfect gas law.

The AUSM solution is the worst. Its values of T fluctuate violently throughout the interval bounded by two shock discontinuities. The maximum deviation ($\doteq$ 12) from the exact solution occurs at $x = 0$. There are also serious overshoots (of T and p) near shock discontinuities. The AUSMD solution is only slightly better. The AUSMV and AUSMDV solutions are much better. Nevertheless, both have a sharp temperature overshoot at $x = 0$. From the above observations and other comparisons,

one may conclude that the CE/SE method is (i) more accurate in shock resolution, and (ii) more capable of preventing a large temperature overshoot at $x = 0$, than any one of the above four upwind schemes.

B. Slowly Moving Contact Surface

The initial conditions at t=0 are:

$$(\rho, p, v) = \begin{cases} (0.125,\ 1.0,\ 0.3\times\sqrt{0.14}) & \text{for } x < 0 \\ (10.0,\ 1.0,\ 0.3\times\sqrt{0.14}) & \text{for } x > 0 \end{cases} \tag{4.2}$$

Note that $c = \sqrt{\gamma p/\rho} = \sqrt{0.14}$ for $x > 0$.

The CE/SE solution at $t = 130\Delta t$ is depicted in Fig. 4. Two solutions at $t = 130\Delta t$ for the same test problem obtained using the AUSMD and AUSMV schemes (CFL= 0.75, and $\Delta x = 1/15$) are depicted in Figs. 3(a) and 3(b) of [3], respectively. The AUSMD solution is comparable to the CE/SE solution in accuracy. However, the values of v in the AUSMV solution has a serious oscillation problem in the interval $(-1, 0)$.

C. Sod's Problem

Sod's problem is solved again in order to compare the CE/SE solution with other solutions presented in [3]. At $t = 0$, we have

$$(\rho, p, v) = \begin{cases} (1.0,\ 1.0,\ 0) & \text{for } x < 0 \\ (0.125,\ 0.1,\ 0) & \text{for } x > 0 \end{cases} \tag{4.3}$$

The CE/SE solution at $t = 50\Delta t$ is plotted in Fig. 5. The solution at $t = 50\Delta t$ for the same test problem obtained using the AUSMDV, AUSM and Roe schemes (CFL=1.0 and $\Delta x = 0.02$) are presented in Figs. 11(a)–(c) of [3], respectively. For each of the above three schemes, it requires about 15 mesh intervals to resolve the contact discontinuity and 2-3 mesh intervals to resolve the shock discontinuity. On the other hand, the CE/SE method requires only 4-5 mesh intervals and 1 mesh interval, respectively, to resolve the contact and shock discontinuities. Moreover, the

numerical errors of the CE/SE solution in the smooth-solution regions are also less than those associated with other three solutions.

D. Strong Expansion Fans

The initial conditions at t=0 are:

$$(\rho, p, v) = \begin{cases} (1.0,\ 2.0,\ -2.5\times\sqrt{2.8}) & \text{for } x < 0 \\ (1.0,\ 0.5,\ 2.5\times\sqrt{2.8}) & \text{for } x > 0 \end{cases} \tag{4.4}$$

Note that $c = \sqrt{\gamma p/\rho} = \sqrt{2.8}$ for $x < 0$.

Assuming CFL=1.0 and $\Delta x = 0.02$, the numerical values of p, ρ and T at $t = 30\Delta t = 0.1025$ for the above test problem obtained using the AUSMDV, Godunov and HILE schemes, respectively, are presented in Figs. 12(a)–(c) in [3]. Because the CE/SE solver with $\epsilon = 0.5, \alpha = 1$ and $\Delta x = 0.02$ is not stable at CFL=1.0, a direct comparison of the CE/SE method with the above three schemes can not be made. Instead, assuming $\epsilon = 0.5, \alpha = 1$ and $\Delta x = 0.02$, we reach for the largest Δt (i.e., the largest CFL because $\Delta x = 0.02$ and $(|v|+c)_{max} = 5.8566$ are known) such that (i) the CE/SE solver is stable, (ii) $n\Delta t = 0.1$ where n is an interger, and (iii) the numerical solution at $t = 0.1$ is such that $p > 0$ and $T > 0$ at all mesh points. Note that $p \leq 10^{-3}$ in the neighborhood of $x = 0.16$. As a result, a numerical undershoot could cause p to become negative. It is found that $\Delta t = 1/550$ (corresponding to $n = 55$ and CFL=0.532) satisfies the above requirements. The corresponding solution is plotted in Fig. 6.

By comparing the CE/SE solution with the Godunov solution which is depicted in Fig. 7, it becomes obvious that the former are far more accurate than the latter. The Godunov's values of T deviate substantially from the exact values in the interval $(-0.5, 0.5)$. The Godunov's values of p also suffer the same order of error percentage-wise although it is difficult to see because the value of p are very small in the same interval. The numerical errors associated with the AUSMDV solution are similar to those of Godunov's solution while the HILE scheme produces even worse results.

In general, the comparison with both the exact and other upwind solutions in this part shows that the current CE/SE Euler scheme can generate highly accurate

shock-tube solutions. Having demonstrated the Euler solver's robust capability of capturing shock and contact discontinuities as well as simulating expansion waves, we are proceeding in the following to extend its application to study the end effects on shock-tube flows.

Test Problems Taken from Ref. 4

In this part, more complex shock-tube problems involving the reflection and intersection of shock waves, expansion waves and contact discontinuities are solved by use of the present Euler solver. The following three test cases are taken from [4] where the exact solutions are also given. The results presented here are obtained with CFL=0.82 in all three cases, whereas the value of Δx is 0.1 in cases E and F but is changed to 0.01 in case G for a more detailed description of the flow.

E. Shock Tube With a Closed End

Consider a strong shock wave traveling at M=4.6 in a constant-area duct filled with air [4, pp.143-144]. When the shock reaches the closed end on the right, it will reflect as described in Fig. 8.

Let the closed end be located at $x = 3.5$, and the initial conditions at t=0 be given as

$$(p, \rho, v) = \begin{cases} (24.52,\ 4.852,\ 4.321) & \text{for } x < 0 \\ (1.0,\ 1.0,\ 0) & \text{for } x > 0 \end{cases} \tag{4.5}$$

Figures 9 and 10 show respectively the results at t=0.5 when the incident shock moves to the right toward the closed end, and at t=1.5 after the shock wave has been reflected and reversed its direction . Other than a slightly lower density observed near the closed end in the reflected wave, the CE/SE solution has excellent agreement with the exact solution at both $t = 0.5$ and $t = 1.5$.

F. Merging of Two Shock Waves

With reference to Fig. 11, consider two shock waves propagating to the right in an infinitely long tube with a strong shock of $M = 3.0$ behind a weaker shock of $M = 1.5$ [4, pp.131-134].

Let the initial conditions at t=0 be

$$(p,\rho,v) = \begin{cases} (25.41,\ 7.189,\ 3.842) & \text{for } x < -1.5 \\ (2.460,\ 1.863,\ 0.821) & \text{for } -1.5 < x < 2.6 \\ (1.0,\ 1.0,\ 0.0) & \text{for } x > 2.6 \end{cases} \tag{4.6}$$

The computed results at t=1.0, 1.25 and 1.75 are shown in Figs. 12–14 in favorable comparison with the exact solution. These two shock waves remain separated before t=1.25. At t=1.25, the faster shock catches up with the slower shock ahead and merging of the two waves begins. As a result of merging, a shock wave stronger than the original faster shock is created and is propagating to the right at a higher speed, leaving behind it a contact surface and a left-moving expansion fan wave, as shown in the plot of Fig. 15 at t=1.75.

G. Shock Tube With Two Closed Ends

This shock tube problem depicted in Fig. 15 constitutes of reflection of shock wave and expansion wave and the intersection of the reflected waves and contact surface. The tube has closed ends at x=0 and x=1, respectively. At t=0, a diaphragm located at x=0.25 separating two gases at different conditions is bursted [4, pp.205-208].

With the initial conditions that

$$(p,\rho,v) = \begin{cases} (20.0,\ 20.0,\ 0.0) & \text{for } x < 0.25 \\ (1.0,\ 1.0,\ 0.0) & \text{for } x > 0.25 \end{cases} \tag{4.7}$$

the break of the diaphragm creates a shock wave and an expansion wave separated by a contact surface .

The calculation is carried out for a period that is long enough to show successive reflection and intersection of shock wave, expansion wave and contact surface. When t= 0.09, waves have not yet reached the ends as shown in Fig. 15. When t=0.3, the left-moving expansion waves have been reflected from the left end but the right-moving shock wave has not . At t=0.4, the shock wave has already completed its reflection from the right end and the reflected shock wave is moving to the left. This

reflected shock is intersecting with the right-moving contact surface to create a left-moving transmitted shock, a right-moving contact surface and a right-moving shock wave which, when reaching the right end, is reflected again. At t=0.585, there exist in the flow field two shock waves, one contact surface and a region of expansion waves. Numerical results plotted in Figs. 16–19 correctly display the aforementioned flow phenomena at those four time instants.

The excellent agreement in all cases demonstrates the ability of the CE/SE scheme to accurately capture weak and strong waves and discontinuities even in the presence of their reflections and intersections. It again verifies the robustness of this scheme.

5. Conclusion

The Space-Time Conservation Element and Solution Element method has been applied to solve the Euler equations. Seven numerical examples on one-dimensional shock-tube flows have been used to demonstrate not only the advantages of simplicity, accuracy and generality of this method, but also its ability of achieving high resolution of discontinuities even in the presence of wave intersections and reflections without any ad hoc techniques. It shows that the CE/SE method is a powerful tool of high potential for solving general fluid dynamic problems. Under investigation is the extension of this method to tackle flow problems of higher dimensions.

Acknowledgment

This work was supported by NASA Lewis Research Center through Grant NAG3-1566.

Bibliography

[1] Chang, S.C., 'New Developments in the Method of Space-Time Conservation Element and Solution Element–Applications to the Euler and Navier-Stokes Equations', NASA TM 106226, August, 1993.

[2] Chang, S.C. and To, W.M., 'A New Numerical Framework for Solving Conservation Laws–The Method of Space-Time Conservation Element and Solution Element', NASA TM 104495, August, 1991.

[3] Wada, Y. and Liou, M.S., 'A Flux Splitting Scheme With High-Resolution and Robustness for Discontinuities', NASA TM 106452, January, 1994.

[4] Rudinger, G., *Wave Diagrams for Nonsteady Flow in Ducts*, Van Nostrand, Princeton, NJ, 1955

Fig. 1 The SEs and CEs of the CE/SE method

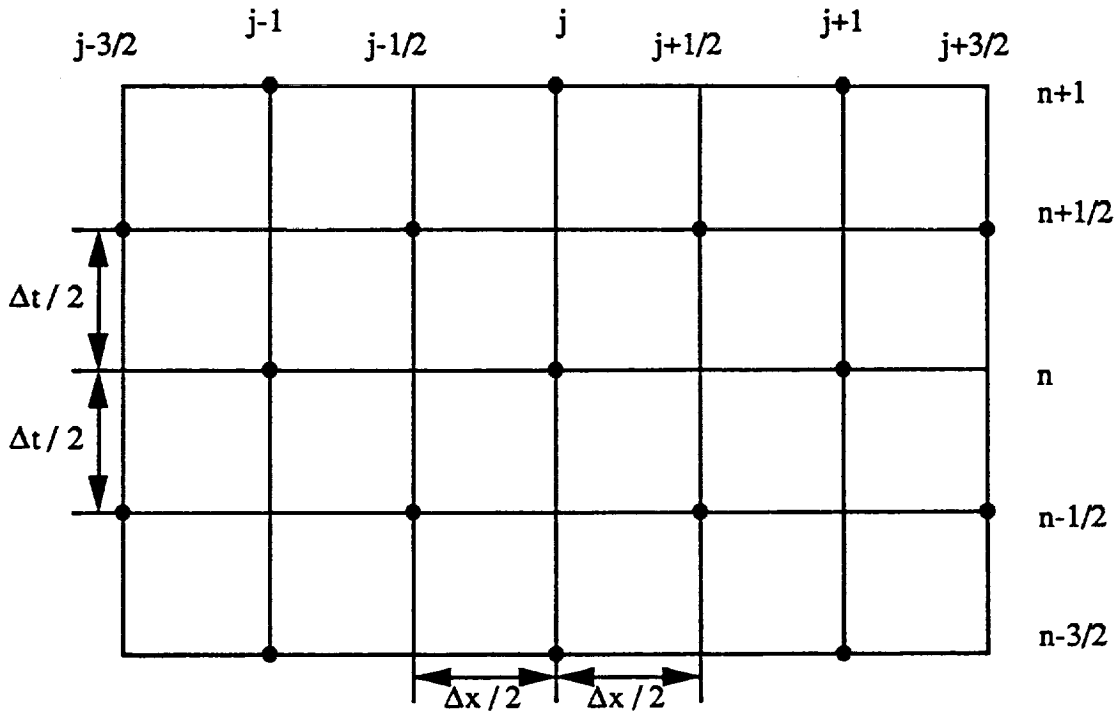

(a) The relative positions of SEs and CEs

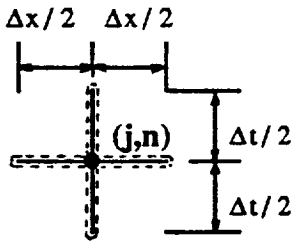

(b) SE(j,n)

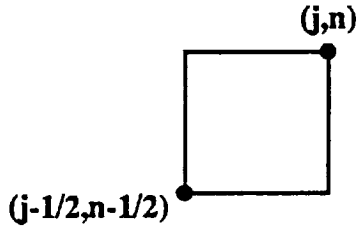

(c) CE_(j,n)

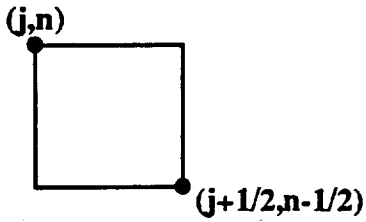

(d) $CE_+(j,n)$

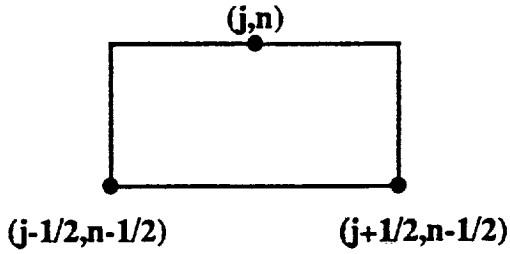

(e) Interior CE(j, n)

Fig. 2 The CE/SE solution for case A at t=100Δt
(CFL=1.0, ΔX=0.02, α=1)

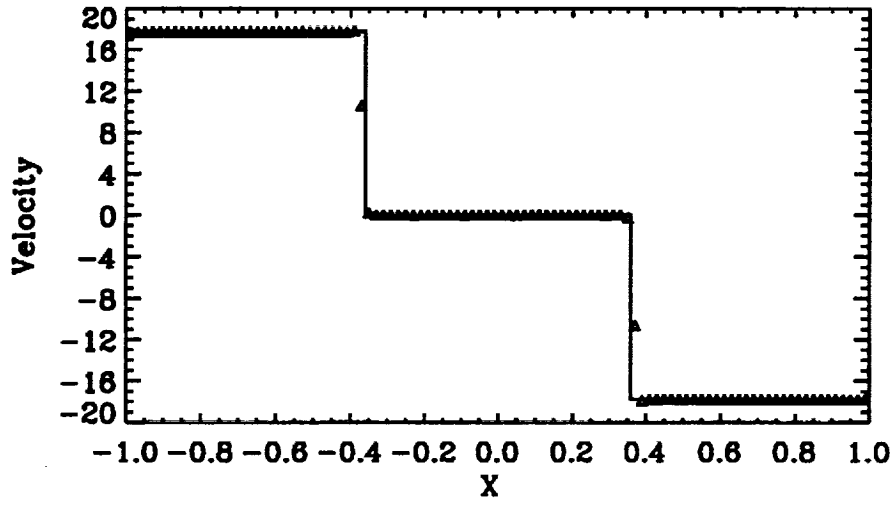

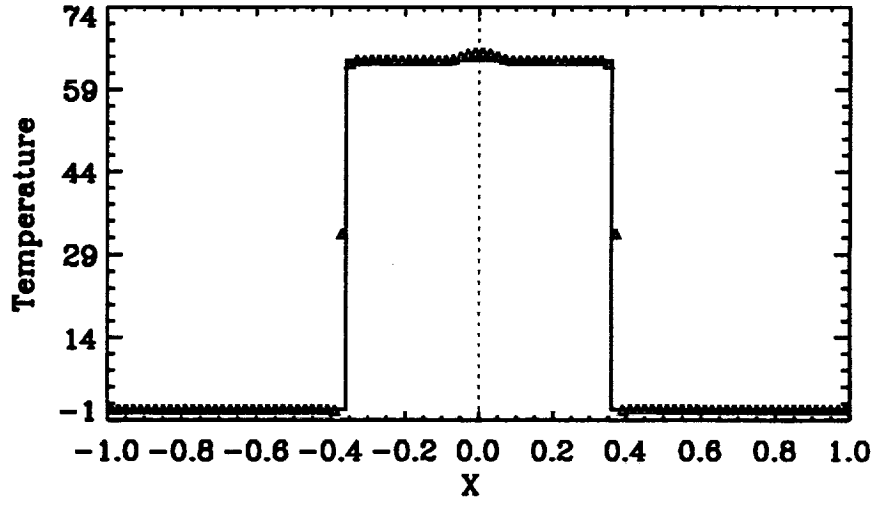

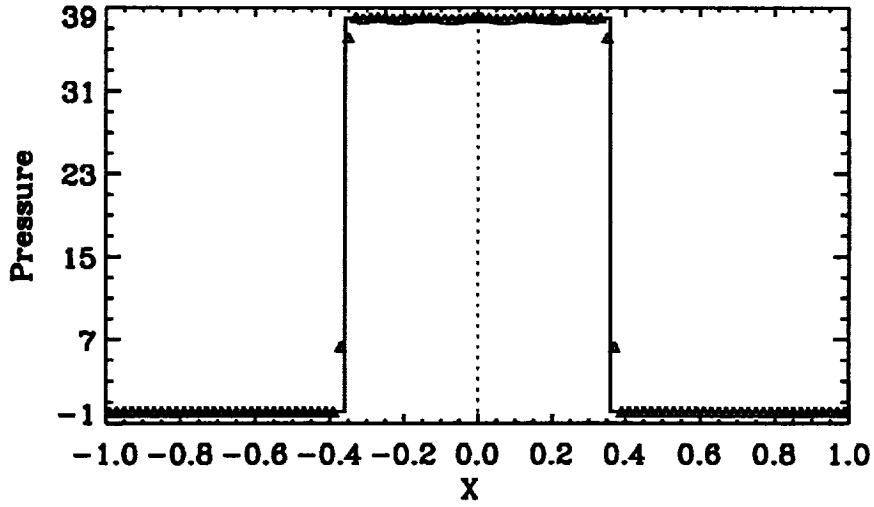

Fig. 3 The CE/SE solution for case A at t=100Δt
(CFL=1.0, ΔX=0.02, α=3)

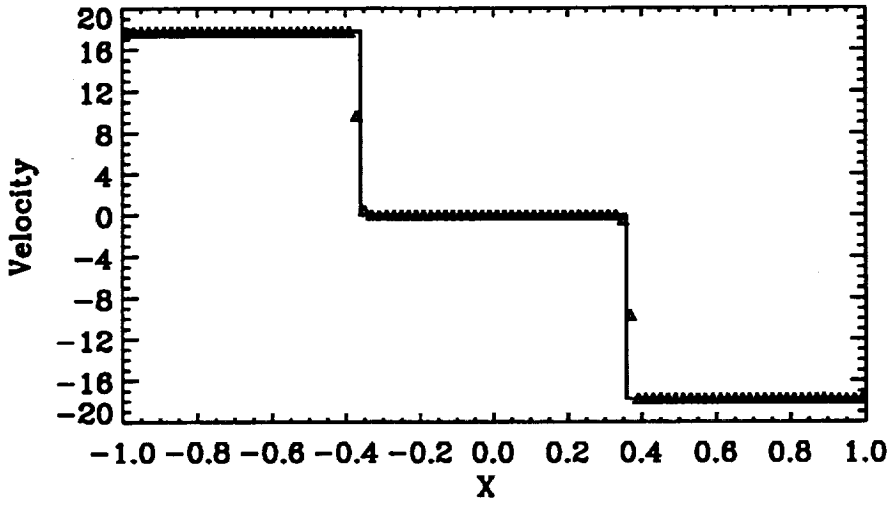

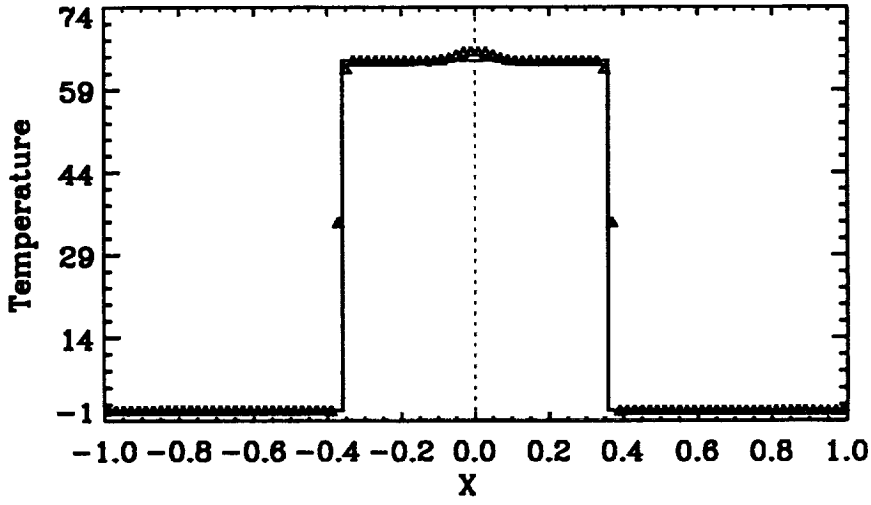

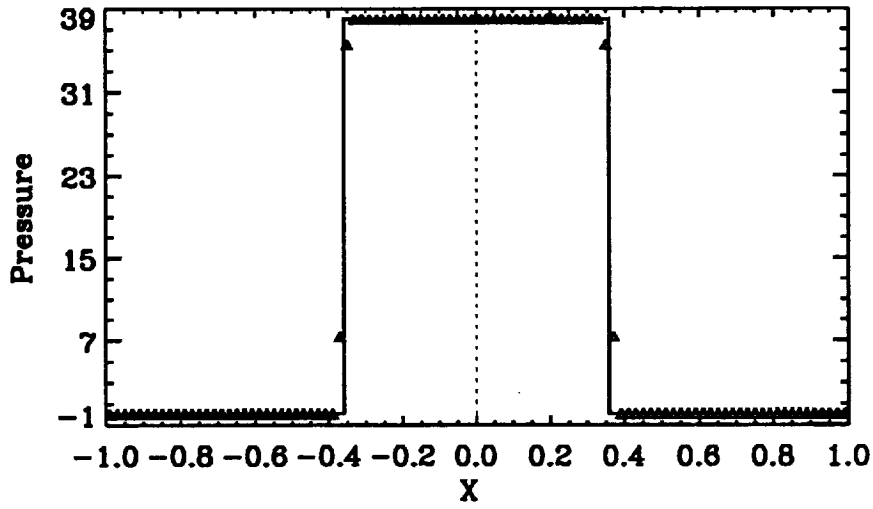

Fig. 4 The CE/SE solution for case B at t=130Δt
(CFL=0.75, ΔX=1/15, α=1)

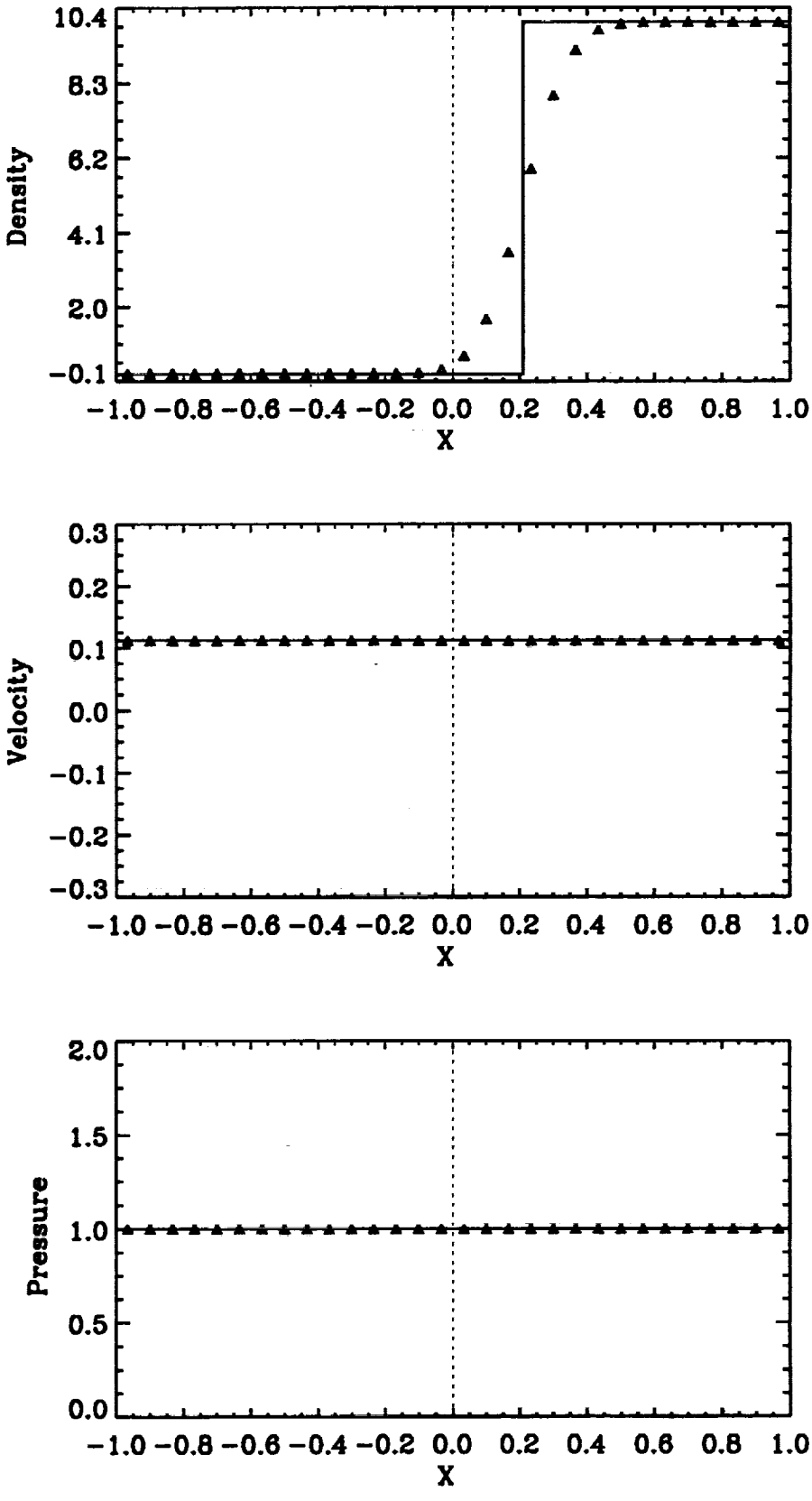

Fig. 5 The CE/SE solution for case C at t=50Δt
(CFL=1.0, ΔX=0.02, α=1)

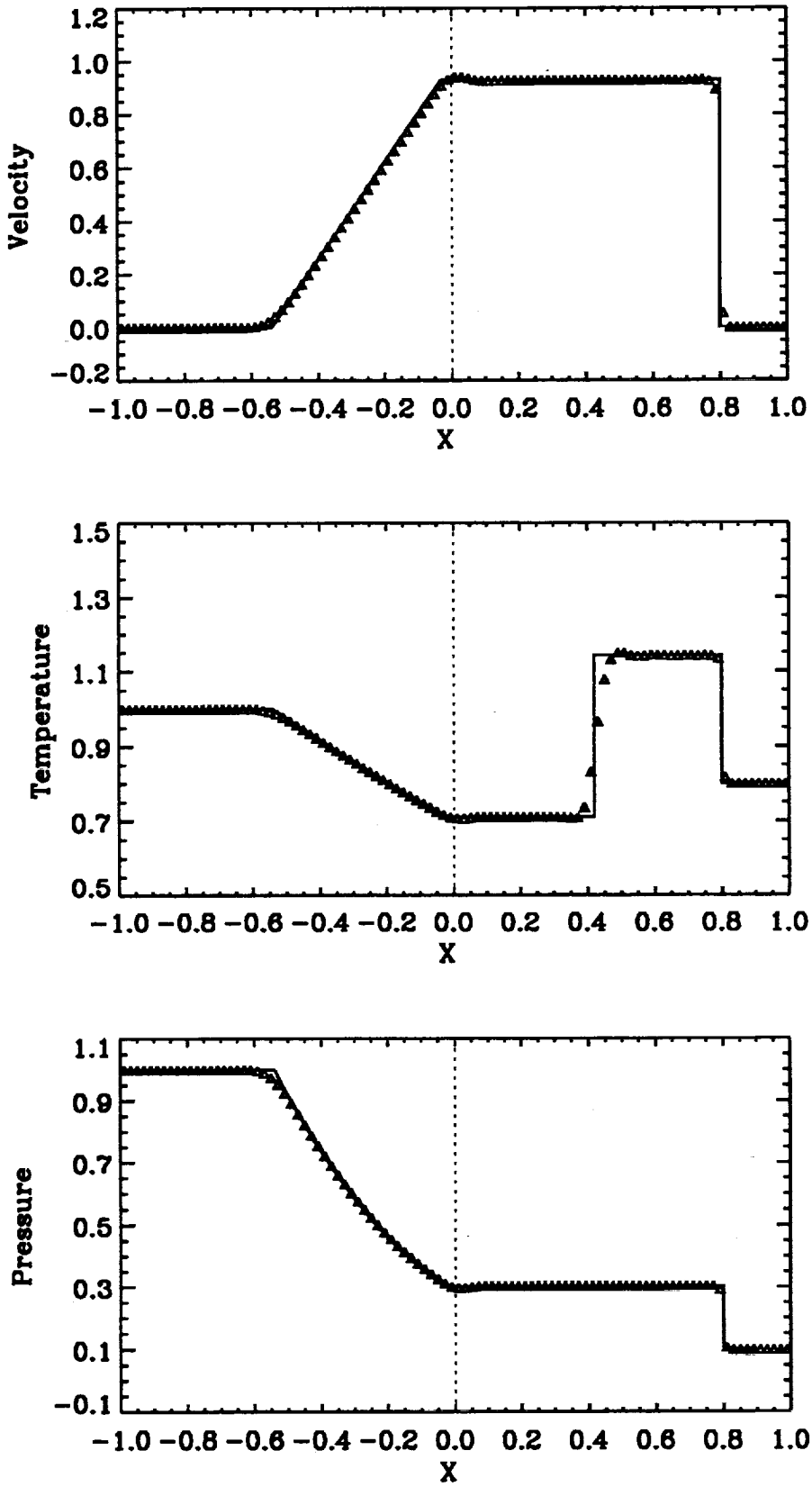

Fig. 6 The CE/SE solution for case D at t=0.1
(CFL=0.532, ΔX=0.02, α=1)

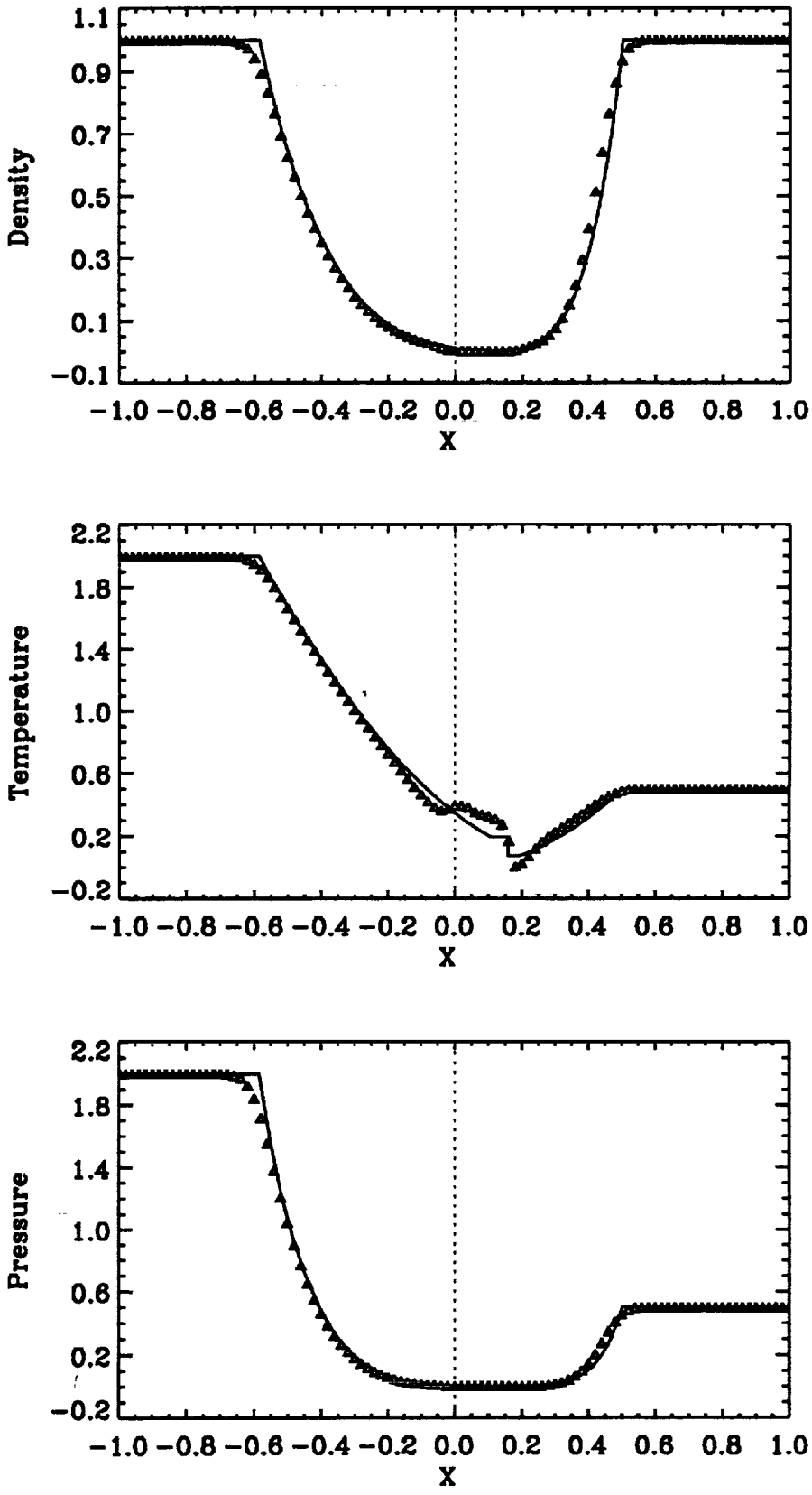

Fig. 7 The Godunov solution for case D at t=0.1025
(CFL=1.0, ΔX=0.02)

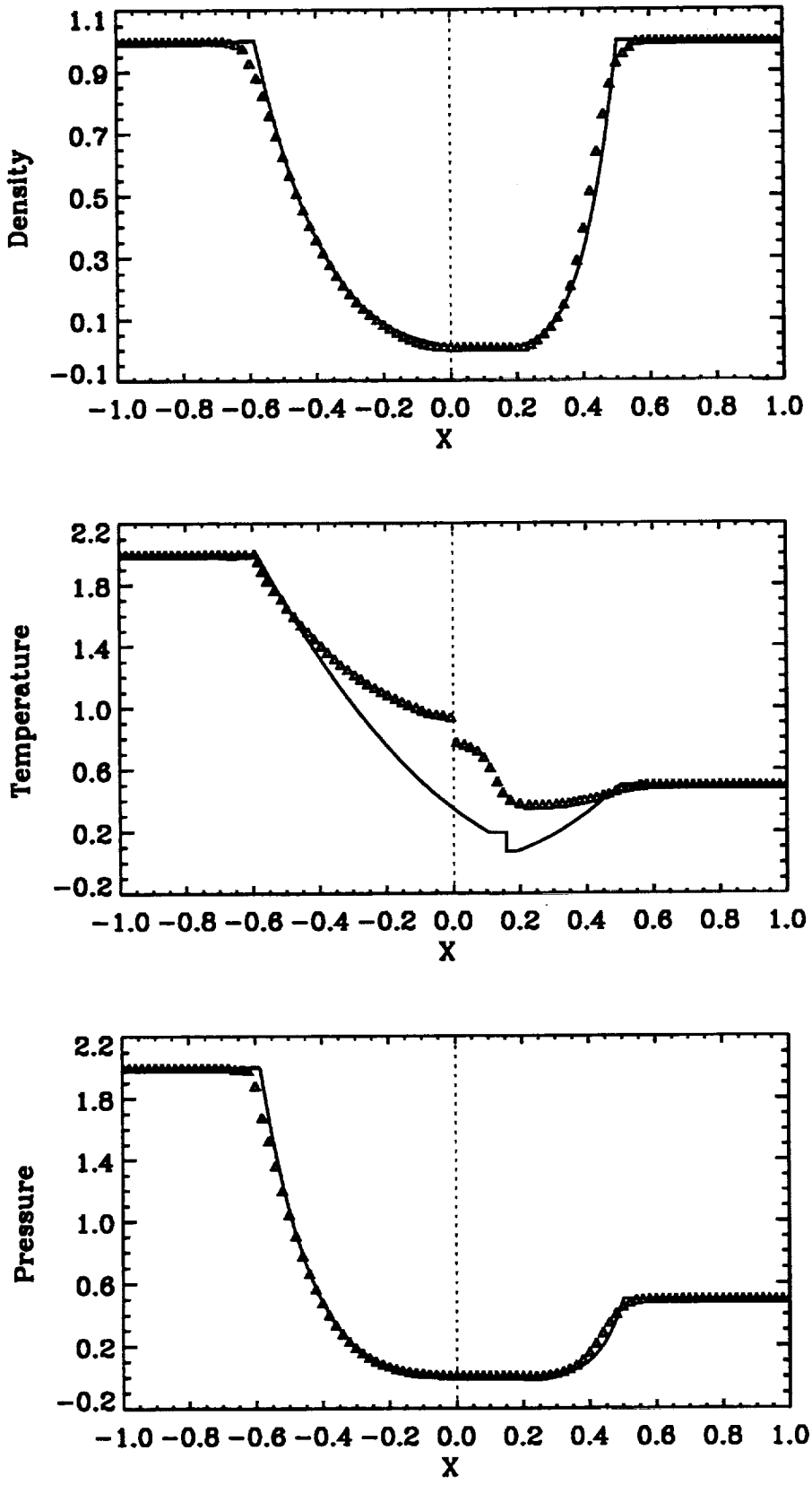

Fig. 8 Shock reflection from a closed end

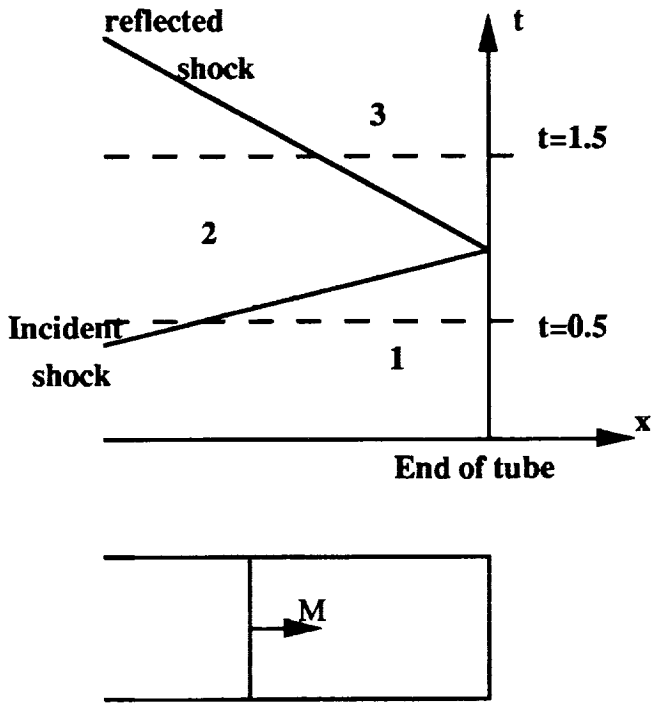

Fig. 9 The CE/SE solution for case E at t=0.5

(CFL=0.82, ΔX=0.1, α=3)

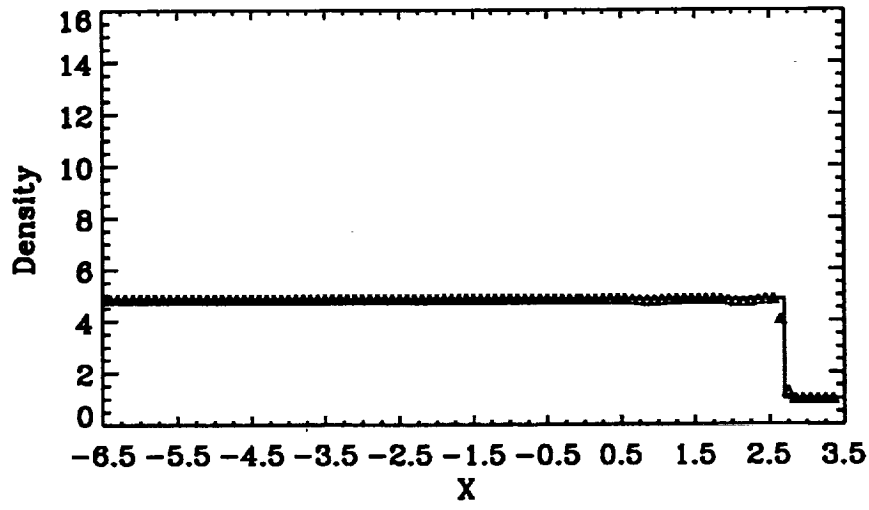

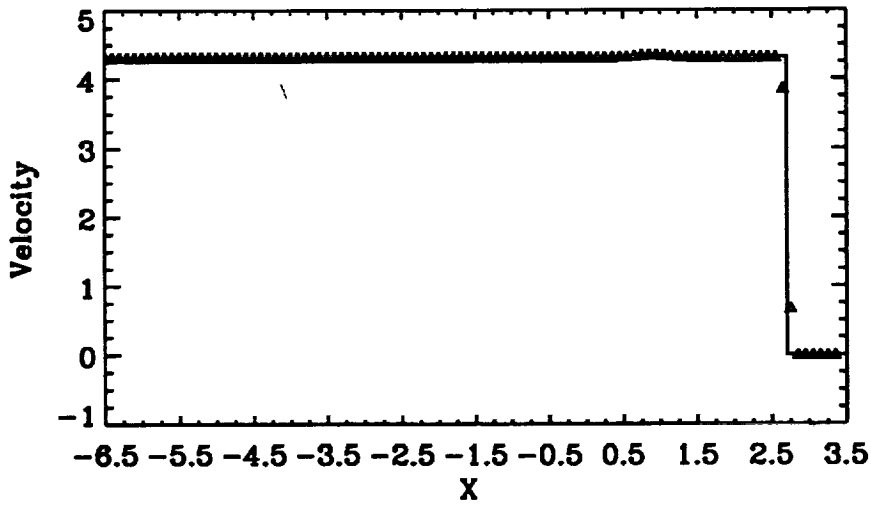

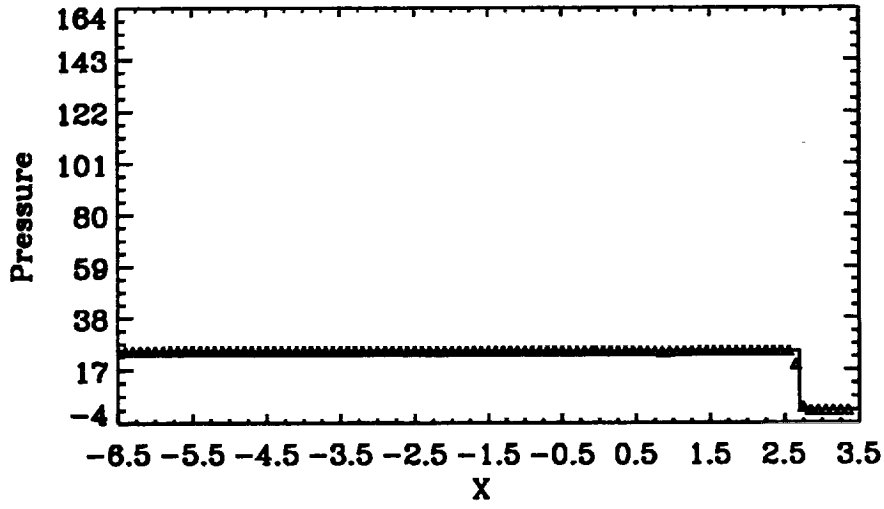

Fig. 10 The CE/SE solution for case E at t=1.5
(CFL=0.82, ΔX=0.1, α=3)

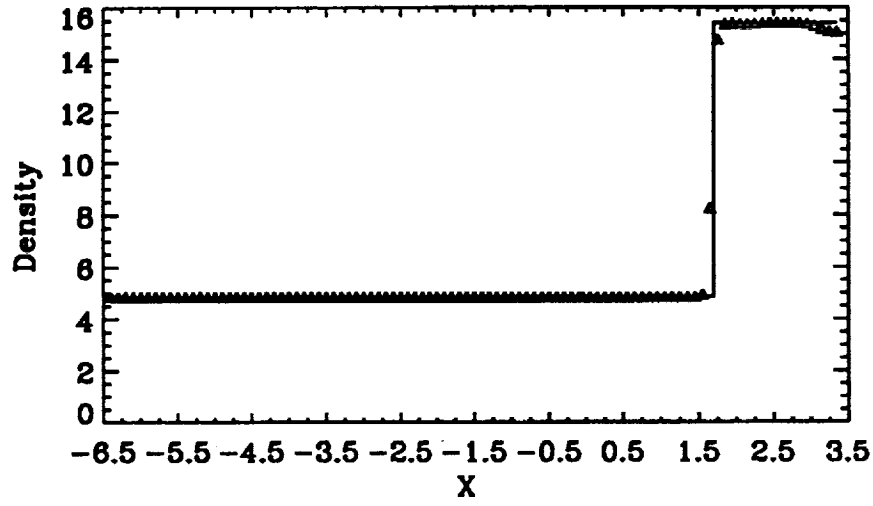

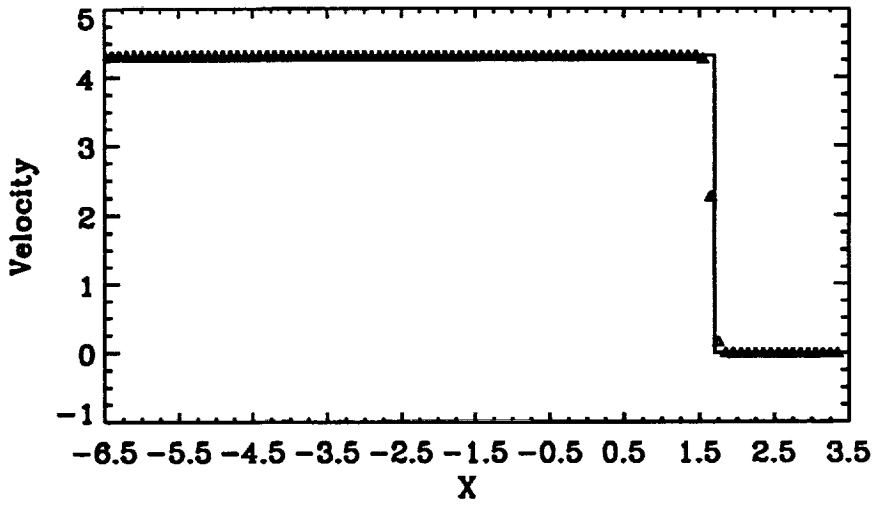

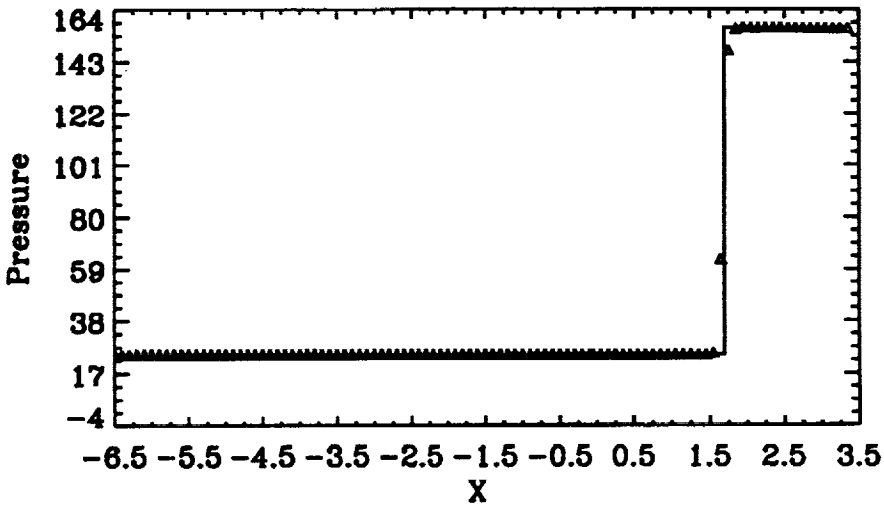

Fig. 11 Merging of two shock waves

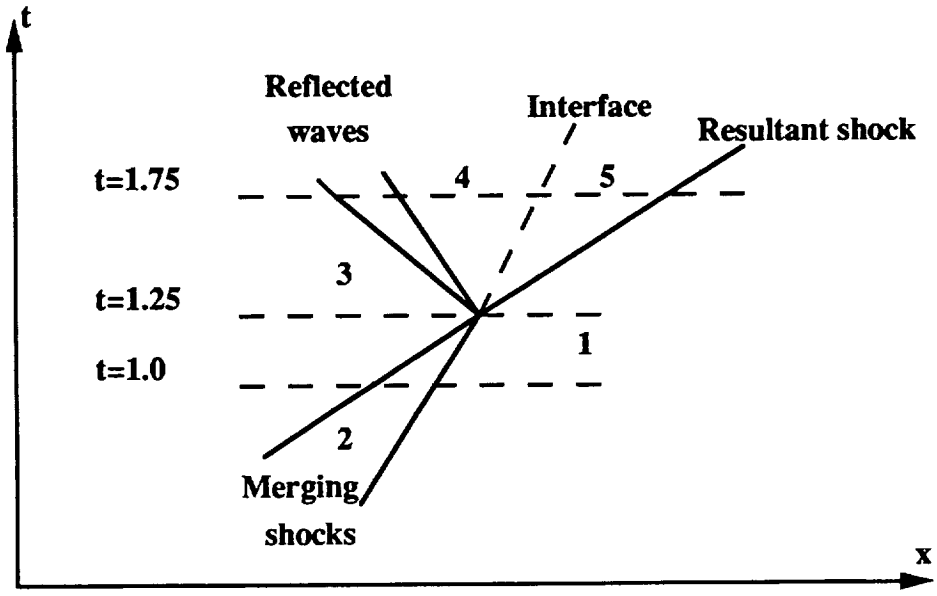

Fig. 12 The CE/SE solution for case F at t=1.0

(CFL=0.82, ΔX=0.1, α=3)

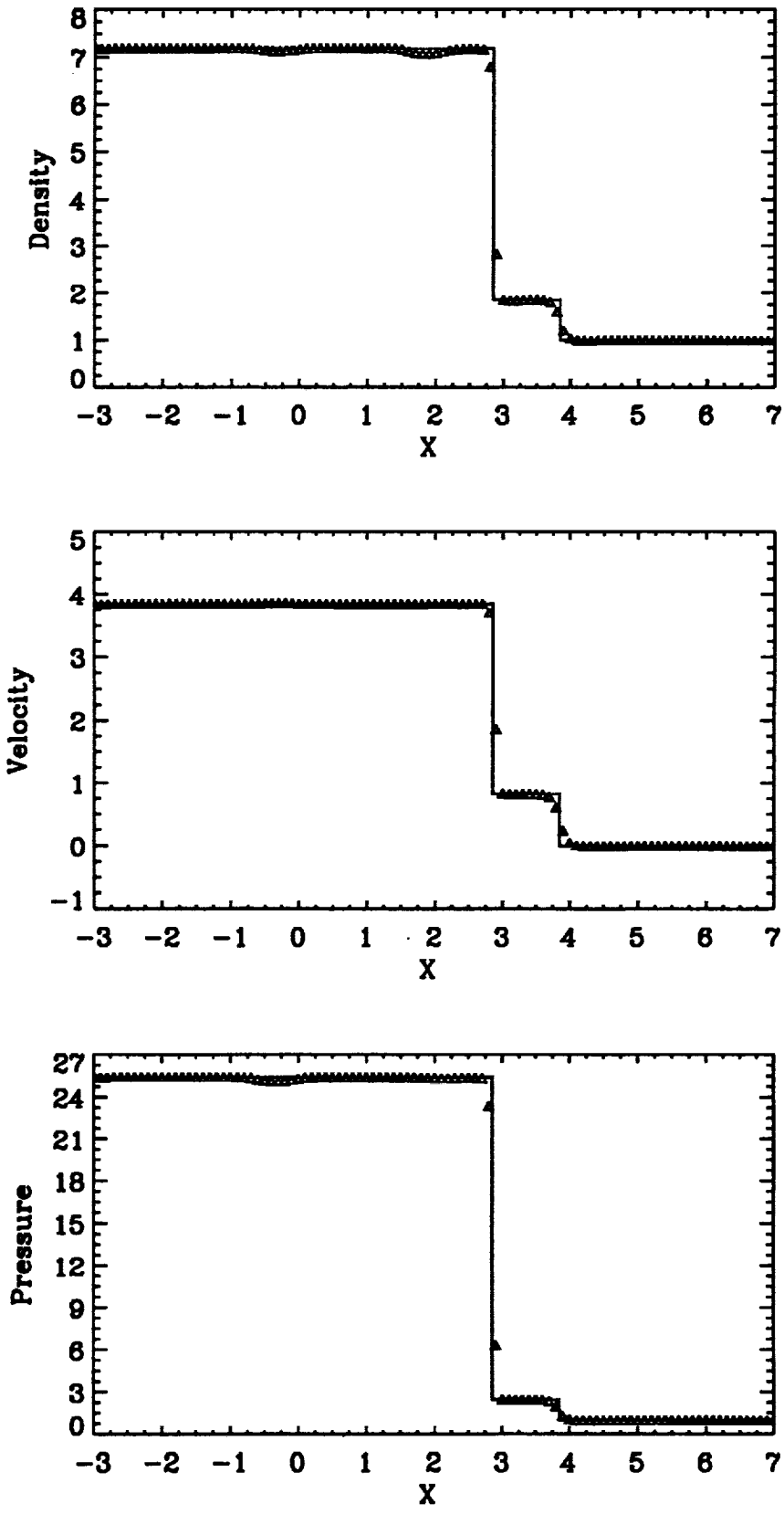

Fig. 13 The CE/SE solution for case F at t=1.25

(CFL=0.82, ΔX=0.1, α=3)

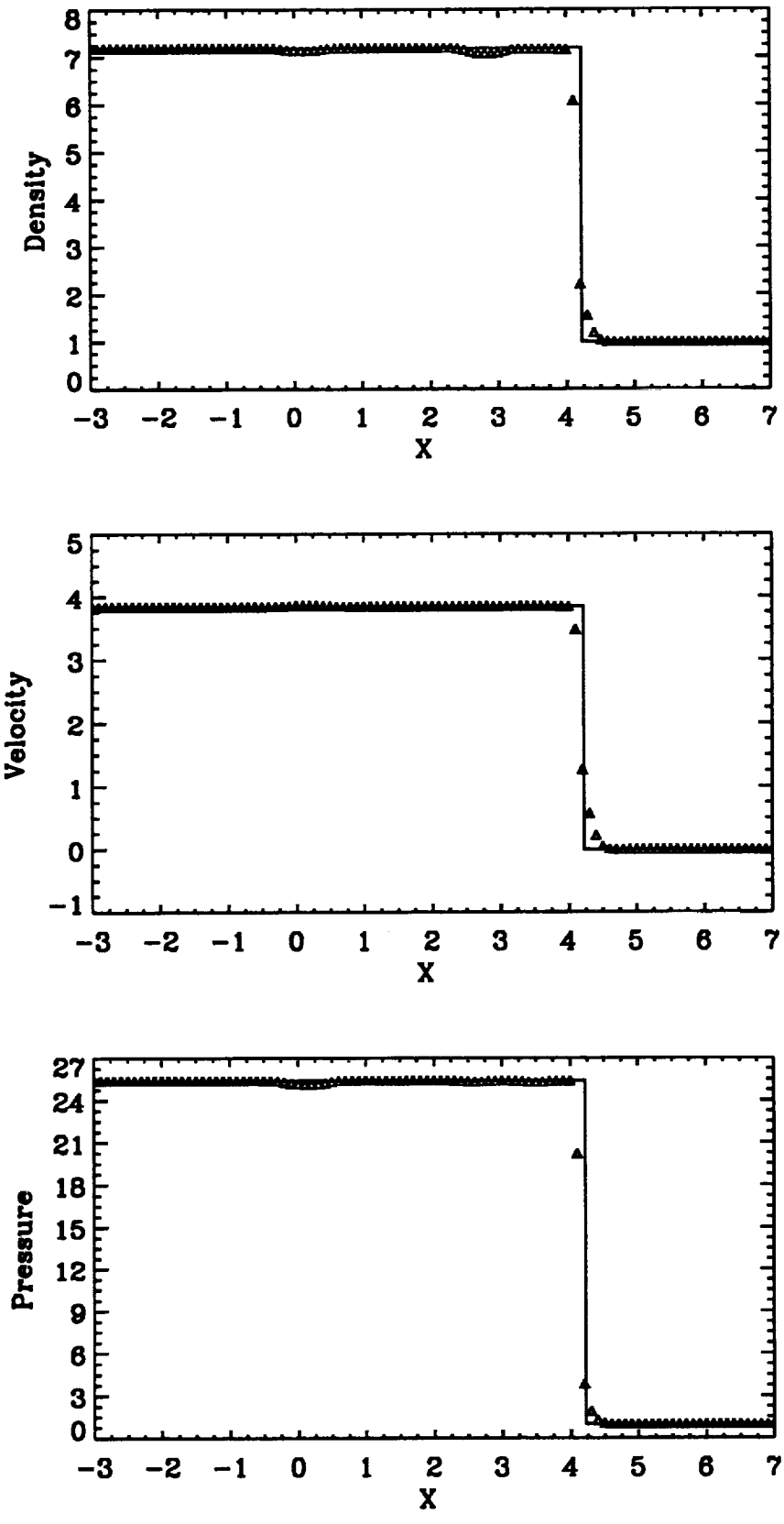

Fig. 14 The CE/SE solution for case F at t=1.75

(CFL=0.82, ΔX=0.1, α=3)

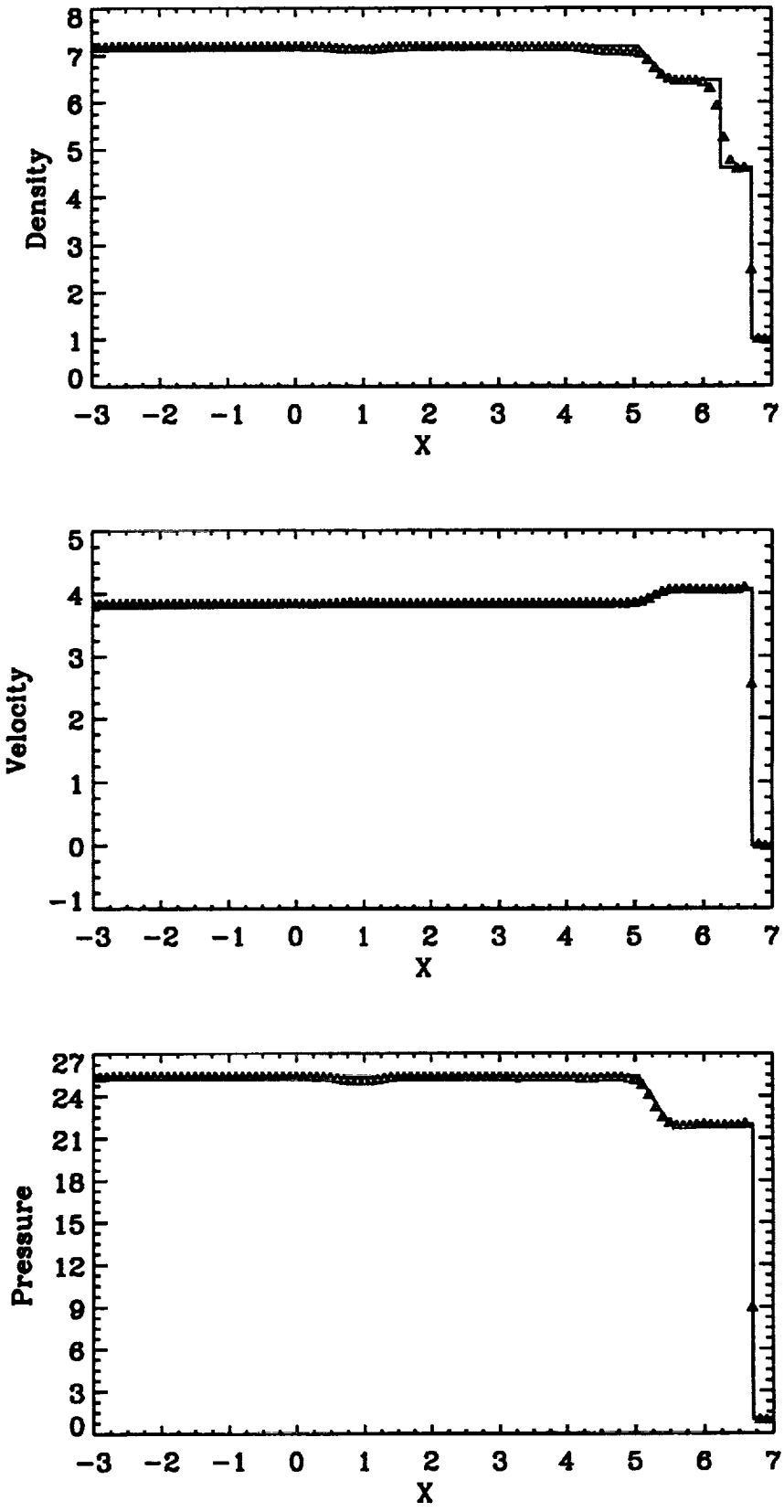

Fig. 15 Shock tube with two closed ends

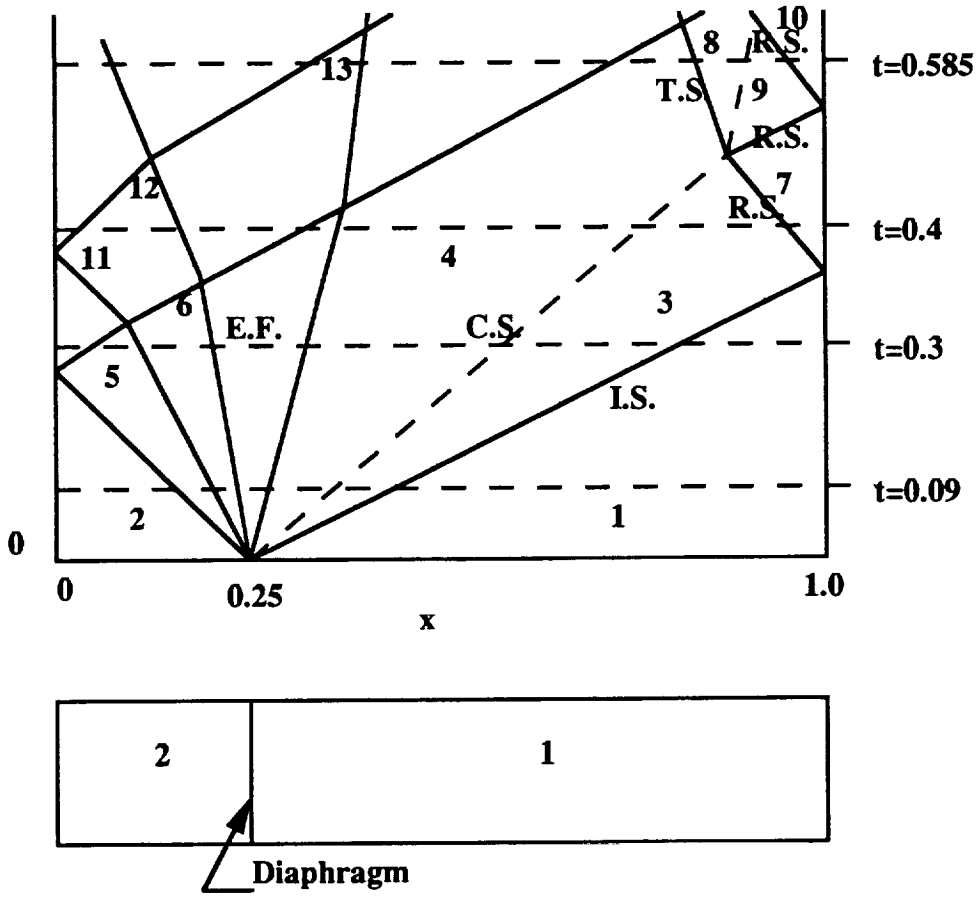

C.S. Contact Surface
E.F. Expansion Fan
T.S. Transmitted Shock
I.S. Incident shock
R.S. Reflected Shock

Fig. 16 The CE/SE solution for case G at t=0.09
(CFL=0.82, ΔX=0.01, α=2)

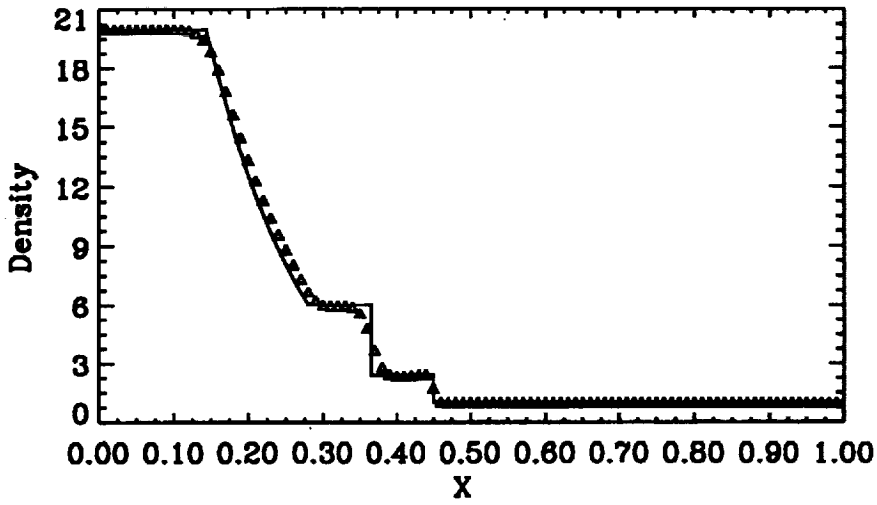

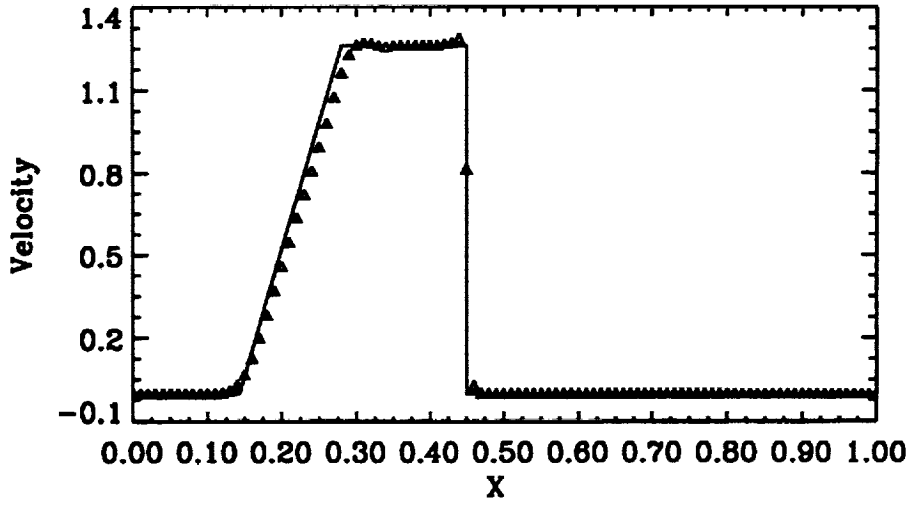

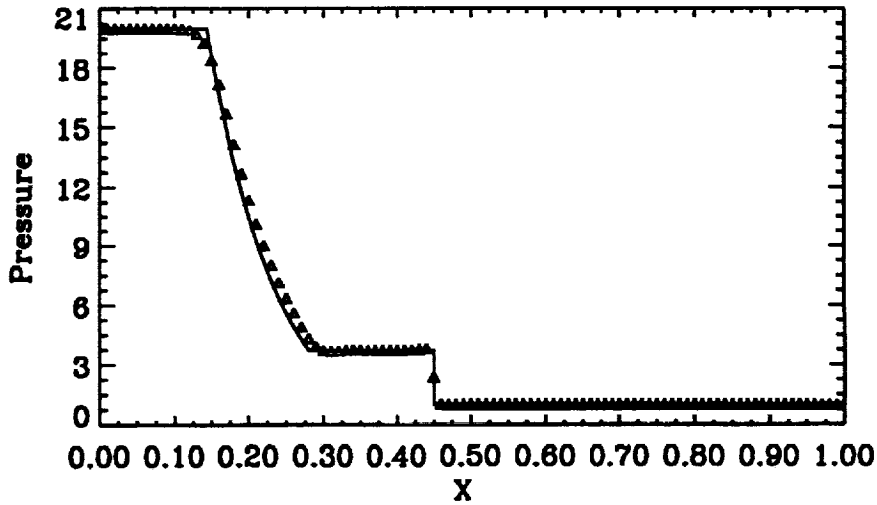

Fig. 17 The CE/SE solution for case G at t=0.3
(CFL=0.82, ΔX=0.01, α=2)

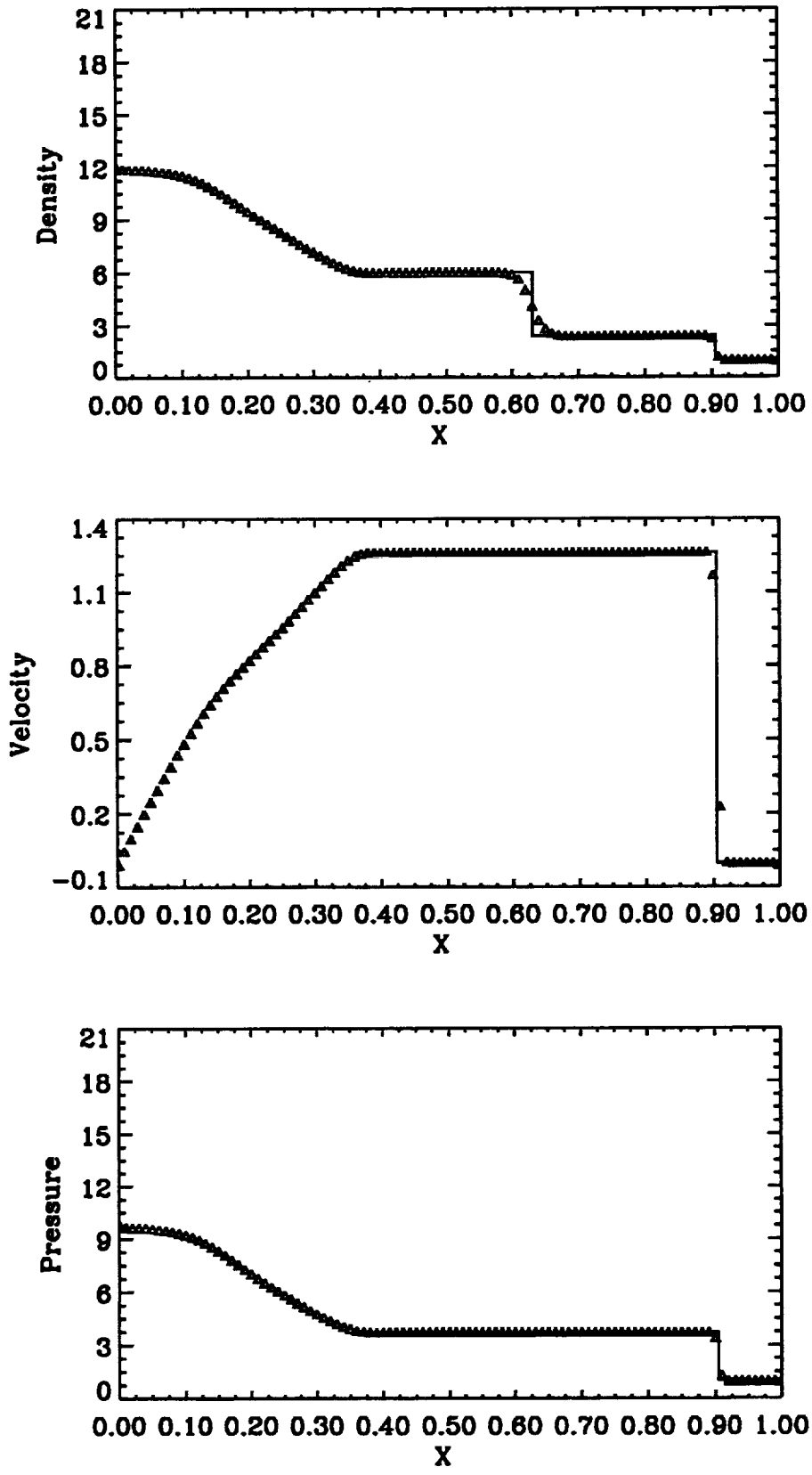

Fig. 18 The CE/SE solution for case G at t=0.4
(CFL=0.82, ΔX=0.01, α=2)

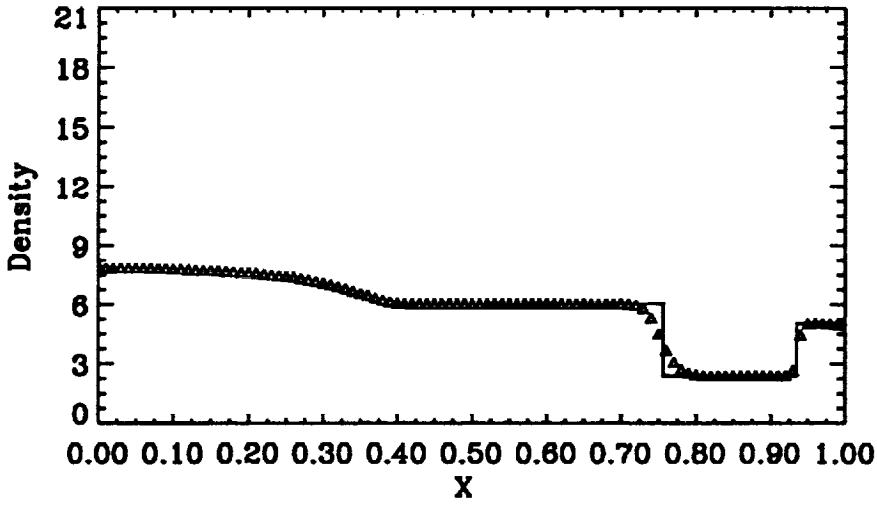

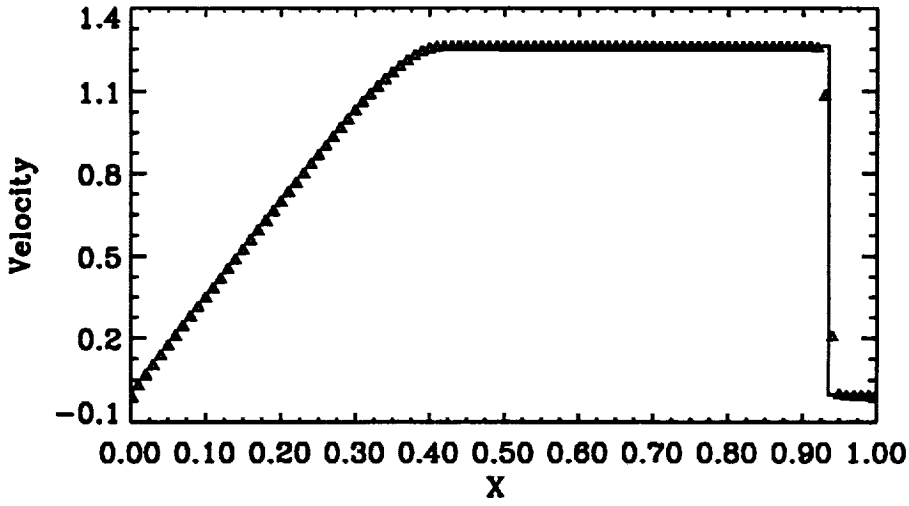

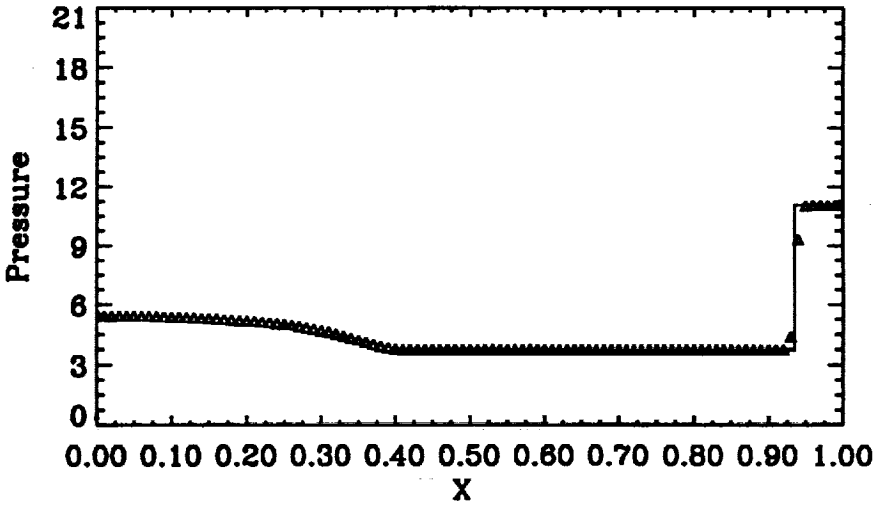

Fig. 19 The CE/SE solution for case G at t=0.585
(CFL=0.82, ΔX=0.01, α=2)

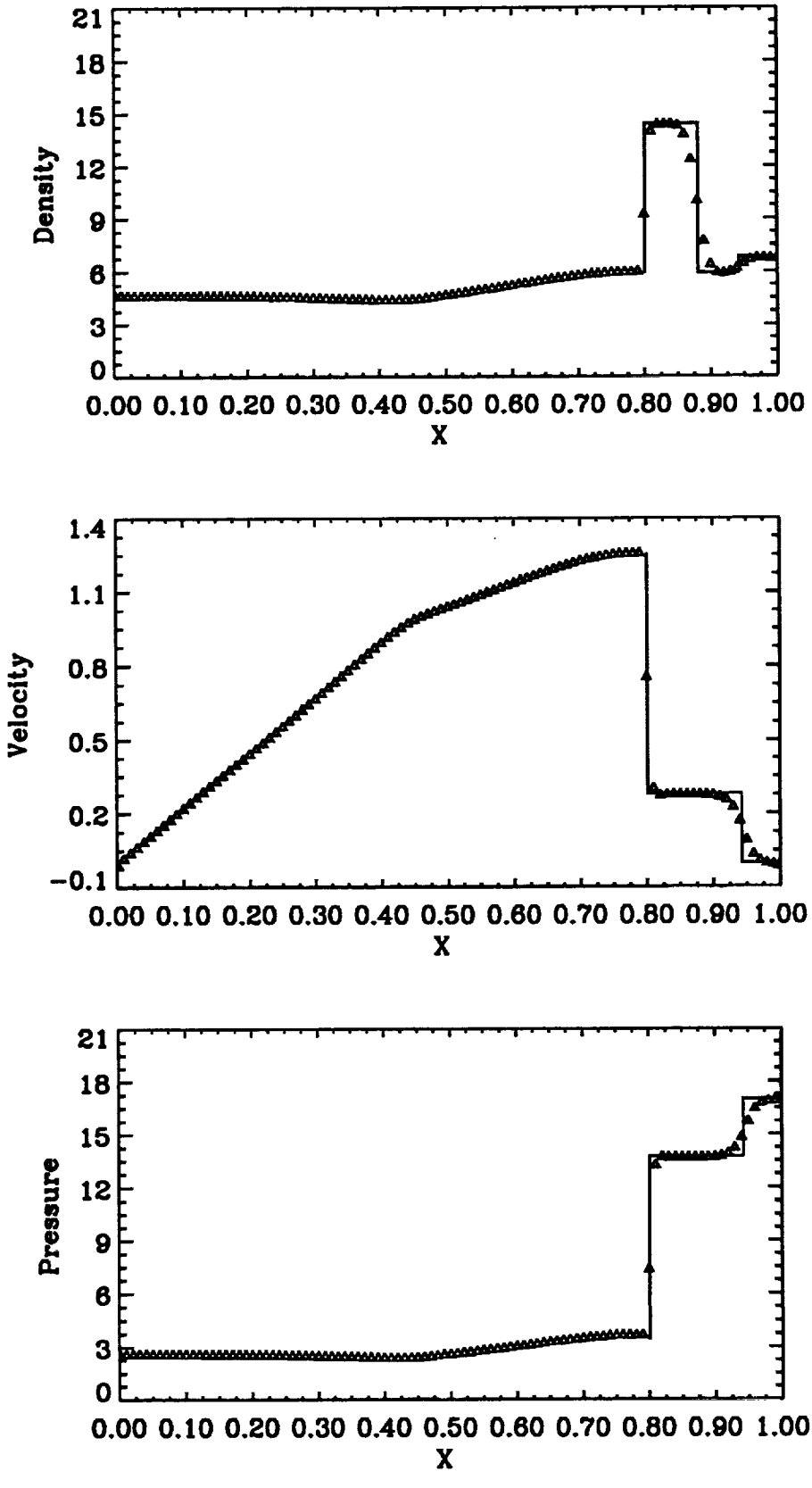

REPORT DOCUMENTATION PAGE

Form Approved
OMB No. 0704-0188

1. AGENCY USE ONLY (*Leave blank*)	2. REPORT DATE	3. REPORT TYPE AND DATES COVERED
	Month 1994	Technical Memorandum

4. TITLE AND SUBTITLE

Application of the Space-Time Conservation Element and Solution Element Method to Shock-Tube Problem

5. FUNDING NUMBERS

WU-505-62-52

6. AUTHOR(S)

Xiao-Yen Wang, Chuen-Yen Chow, and Sin-Chung Chang

7. PERFORMING ORGANIZATION NAME(S) AND ADDRESS(ES)

National Aeronautics and Space Administration
Lewis Research Center
Cleveland, Ohio 44135-3191

8. PERFORMING ORGANIZATION REPORT NUMBER

E-9288

9. SPONSORING/MONITORING AGENCY NAME(S) AND ADDRESS(ES)

National Aeronautics and Space Administration
Washington, D.C. 20546-0001

10. SPONSORING/MONITORING AGENCY REPORT NUMBER

NASA TM-106806

11. SUPPLEMENTARY NOTES

Xiao-Yen Wang and Chuen-Yen Chow, Department of Aerospace Engineering Sciences, University of Colorado at Boulder, Boulder, Colorado 80309-0429; Sin-Chung Chang, NASA Lewis Research Center. Responsible person, Sin-Chung Chang, organization code 2660, (216) 433-5874.

12a. DISTRIBUTION/AVAILABILITY STATEMENT

Unclassified - Unlimited
Subject Categories 34 and 64

This publication is available from the NASA Center for Aerospace Information, (301) 621-0390.

12b. DISTRIBUTION CODE

13. ABSTRACT (*Maximum 200 words*)

An Euler solver based on the method of space-time conservation element and solution element is used in this paper to simulate shock-tube flows involving shock waves, contact discontinuities, expansion waves and their intersections. Seven test problems are considered to examine the capability of this method. The numerical results, when compared with exact solutions and/or numerical solutions by other methods, indicate that the present method can accurately resolve strong shock and contact discontinuities without using any ad hoc techniques which are used only at the neighborhood of a discontinuity.

14. SUBJECT TERMS

Space-time; Conservation element; Solution element; Shock tube

15. NUMBER OF PAGES

37

16. PRICE CODE

A03

17. SECURITY CLASSIFICATION OF REPORT	18. SECURITY CLASSIFICATION OF THIS PAGE	19. SECURITY CLASSIFICATION OF ABSTRACT	20. LIMITATION OF ABSTRACT
Unclassified	Unclassified	Unclassified	

National Aeronautics and
Space Administration

Lewis Research Center
21000 Brookpark Rd.
Cleveland, OH 44135-3191